Numerical and experimental characterization of a piezoelectric actuator for microfluidic cell sorting

Cristian Brandi [a],[1], Adele De Ninno [b],[1], Enrico Verona [b], Luca Businaro [b], Paolo Bisegna [a], Federica Caselli [a],[*]

[a] *Department of Civil Engineering and Computer Science, University of Rome Tor Vergata, Rome, Italy*
[b] *Institute for Photonics and Nanotechnology, Italian National Research Council, Rome, Italy*

ABSTRACT

Piezoelectric actuators offer great opportunities for precise and low-cost control of fluids at the microscale. Microfluidic systems with integrated piezoelectric actuators find application as droplet generators, micropumps, and microsorters. To accelerate device design and optimization, modeling and simulation approaches represent an attractive tool, but there are challenges arising from the multiphysics nature of the problem. Simple, potentially real-time approaches to experimentally characterize the fluid response to piezoelectric actuation are also highly desirable. In this work, we propose a strategy for the numerical and experimental characterization of a piezoelectric microfluidic cell sorter. Specifically, we present a 3D coupled multiphysics finite-element model of the system and an easy image-based approach for flow monitoring. Sinusoidal and pulse actuation are considered as case studies to test the proposed methodology. The results demonstrate the validity of the approach as well as the suitability of the system for cell sorting applications.

1. Introduction

Cell sorting is the process of separation of target cell populations from a heterogeneous mixture and represents a critical enabling technology in cell-based diagnostics and therapies [1,2]. Progress in the field of microfluidics has facilitated the realization of miniaturized devices for selective separation of cells, offering advantages such as low sample volume and possibility for high integration and combination with downstream processes [3,4].

Two main categories of microfluidic cell sorters can be identified [2]: large amount sorting and precise sorting. Whereas large amount sorting lacks single-cell resolution and is generally used for enriching cell populations (e.g., circulating tumor cells [5,6]), precise sorting can direct the cells into a target channel one by one (i.e., single cell sorting). Microfluidic systems for precise sorting usually include two components: a sensor, to identify target vs non-target cells, and an actuator, to direct target cells into specific outlets. Whereas a common sensing approach is the optical detection of fluorescently labelled cells [7–9], electrical detection approaches represent an attractive alternative due to their label-free nature [10–13]. Regarding the actuation, several

methods have been explored (see e.g., the review [2] and the references therein), including acoustophoresis [14], dielectrophoresis [15], optical methods [16], vapor bubble actuators [17], and piezoelectric actuators [18–20].

As shown in a seminal paper by Chen et al. [7], a microfluidic cell sorter with integrated piezoelectric actuator has several interesting features, including low cost, low voltage (~ 10 V_{pp}) and low power consumption (0.1 mW), precise control of the magnitude of transverse cell deflection, and short reaction time (0.1–1 ms). Chen et al. [21] used a compact microfluidic fluorescence-activated cell sorting (μFACS) platform with an integrated piezoelectric actuator for isolation of rare bacteria from microbial samples. Zhao et al. [22] employed a similar system to pre-screen libraries of variants of a yellow fluorescence-protein-based Ca^{2+} indicator. Cheng et al. [8] demonstrated a μFACS microchip integrated with two piezoelectric actuators for automated, high-performance mammalian cell analysis and enrichment.

External piezoelectric actuators, requiring higher voltage (~ 100 V_{pp}), were also reported. Sakuma et al. [23] proposed a high-throughput sorting method for large cells using dual membrane pumps

---

synchronously activated by external piezoelectric actuators. Cai et al. [24] presented a new design of amplified piezoelectrically actuated microvalve and applied it to demonstrate an on-chip flow-switching-based sorting mechanism. Shemesh et al. [25] presented a piezoelectric-driven droplet sorter that is simple to fabricate, reproducible, and robust.

Modeling and simulation approaches are extremely useful to accelerate the design and optimization of microfluidic devices [26–29]. In the context of microfluidic systems endowed with piezoelectric actuators, modeling of piezoelectric micropumps has been reported in several works. In order to optimize the design of a peristaltic pump integrated into a microfluidic chip, Bu et al. [30] derived an analytical formula for calculating the maximum deflection of a circular membrane driven by a piezoelectric disc. Ma et al. [31] used a simplified fluidic circuit model to calculate the transported volume in a peristaltic micropump consisting of a microchannel and three piezoelectric actuators. A one-way coupled simulation of fluid motion in a piezoelectric valveless pump was presented by Rojas and Morales [32], by using a simplified symmetric 3D pump model. A fully coupled multiphysics simulation (solid mechanics, electrostatic, and fluid flow) was presented by Holman et al. [33] to characterize a piezoelectric actuated micropump with integrated elastomeric check valves. A 2D geometry was used in that work, to reduce the complexity of a 3D geometry and to decrease the computation cost. Yazdi et al. [34] used a 3D two-way fluid-structure interaction model to optimize the geometrical features of a piezoelectric micropump for biomedical applications. Shimizu et al. [35] used a 3D fluid-structure and electric coupled analysis to verify the pumping and mixing performance of a metal-capped piezoelectric actuator.

By comparison, modeling and simulation of microfluidic sorters based on piezoelectric actuators has been less explored. A 2D fluid dynamic model was used by Shemesh et al. [25] to investigate droplet sorting based on the ratio between the flow rate out of the piezoelectric sorter and the flow rate introduced at the main channel entrance. Chen et al. [7] used computational fluid dynamics and particle tracing to study a piezoelectric cell sorter, by modelling the piezoelectric actuation as a time-dependent sinusoidal pressure.

Alongside with numerical tools for in-silico analysis and design, experimental approaches to monitor the fluid response to piezoelectric actuation in the actual device are needed. Typically, in microfluidic cell sorters, the cell suspension (sample) is centrally focused along the microchannel by means of lateral sheath flows and the actuator displacement induces a deflection of the sample stream, which displaces the selected cell towards the desired outlet. If the sample fluid and the sheath fluid have different optical properties, the deflection of the sample stream can be visualized using a microscope [36,37]. Image snapshots representative of different stream deflections can easily be acquired, however a quantitative analysis of the flow switching performance requires a tailored image processing approach. Simple, potentially real-time approaches are particularly attractive since they can enable closed-loop control of the actuator drive signal.

In this work, we present an original approach for the numerical and experimental characterization of a microfluidic piezoelectric actuator for cell sorting. Specifically, we develop: (i) a 3D coupled multiphysics (electrical-structural-fluidic) finite element model of the microfluidic system; (ii) a simple image-based approach to experimentally quantify the deflection of the sample stream. Sinusoidal and pulse actuation are considered as case studies to illustrate the proposed method.

The paper is organized as follows. The microfluidic device and the experimental setup are introduced in Section 2. The finite element model of the device and the image-based approach for sample deflection analysis are presented in Section 3 and Section 4, respectively. The results of the numerical and experimental characterization are described in Sections 5.1 and 5.2, respectively. Discussion and conclusion are reported in Section 6.

2. Microfluidic device and experimental setup

The device considered in this work is shown in Fig. 1. It is realized in a polydimethylsiloxane (PDMS, Dow Corning) block, fabricated by soft-lithography methods, and sealed to a 56 mm × 75 mm glass slide (Fig. 1 (a)). The fluidic layout is as follows (Fig. 1(b)): the sample suspension is delivered into the main channel through inlet I_1; two lateral sheath flows, delivered through the common inlet I_2, are used to focus the sample flow; three channels are present after the sorting region, ending in outlets O_1 (central channel), O_2 (left channel), and O_3 (right channel). Two oval-shaped lateral regions are designed on the sides of the sorting region. The lateral region on the left houses a cylindrical chamber above which a circular piezoelectric transducer (Mouser Electronics) is bonded. As bonding strategy, we exploited a mercaptosilane coupling reagent as molecular adhesive between the transducer and the PDMS surfaces [38]. Specifically, the transducer is coated by a MPTS (3 mercaptopropyl trimethoxy silane) solution and then oxygen plasma-activated together with the assembled chip. Under a stimulation voltage, the piezoelectric transducer bends proportionally to the applied potential. In case of downward deflection, an amount of fluid (in the order of tens of nL) is pumped into the sorting region, thus deflecting the sample stream towards outlet O_3. Conversely, in case of upward deflection the sample stream is deflected towards outlet O_2.

As shown in Fig. 1(c), the main channel is 150 μm wide, while the width of the three collection channels is 50 μm each. The lateral region nozzles are 100 μm in width, with a distance from the diverging junction of about 50 μm. Microchannel height is 40 μm. The cylindrical chamber is 13 mm in diameter and 5 mm in height. The transducer is made of a lead zirconate titanate (PZT) element of 15 mm diameter and 110 μm thickness, having a metal substrate (brass) of 20 mm diameter and 100 μm thickness.

For the experimental characterization of the piezoelectric actuator, a buffer made of PBS (Phosphate-Buffered Saline), 13% sucrose, and 0.1% Tween 20 was pumped into inlet I_1 (sample flow) with a syringe pump (Elite 11, Harvard Apparatus) at 5 μl/min. That buffer is commonly used in microfluidic impedance cytometry [39,40]. The sheath flows (deionized water) were delivered through inlet I_2 using a pressure controller (OB1, Elveflow). Typical pressure values were around 300 mbar, yielding a flux of about 15 μl/min.

The microfluidic device was mounted on the stage of an inverted microscope (Zeiss Axio Observer, 10 × objective) and the fluid flow through the sorting region was acquired using a high-speed camera (Photron Mini UX100, frame rate 4000–16000 fps based on actuation frequency, shutter time 25 μs) connected to the microscope. With the present setup, the sample flow was optically distinguishable from the sheath flows (cf. Section 4).

The piezoelectric transducer was driven by a waveform generator (Keysight 33600A). Both sinusoidal actuation (3, 15, 25, 50, 75, or 100 Hz frequency) and pulse actuation (20, 10, 5, 1, or 0.5 ms pulse duration) were used. The typical value of the applied potential was 10 V_{pp} or lower.

3. Finite element model for in-silico device analysis

3.1. Device geometric model

The geometric model of the device, shown in Fig. 2(a-c), consists of a solid domain (Ω_s) and a fluid domain (Ω_f). The solid domain Ω_s is divided into the PZT element (Ω_p), the metal substrate (Ω_m), and the PDMS (Ω_{PDMS}). The fluid domain (Fig. 2(b)) includes a portion (8 mm) of the main channel, the sorting region, the three collection channels, and the left oval-shaped lateral region, which houses the cylindrical chamber. The sample flow and the sheath flows were not differentiated. As a matter of fact, the length of the hydrodynamic entrance region is in the order of tens of microns (cf. e.g., [41]) and therefore, after the confluence of the sample and sheath flows, a fully developed laminar
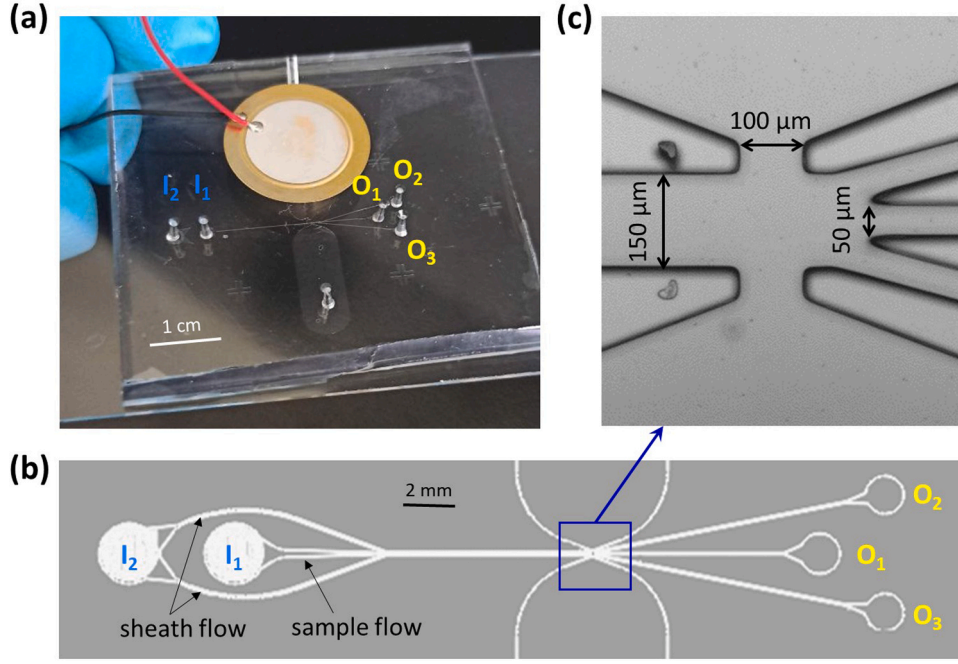
Fig. 1. (a) Device photograph and (b) fluidic layout, with indication of inlets (I_1,I_2) and outlets (O_1,O_2,O_3). (c) Microscopy image of the sorting region of the device, with indication of relevant dimensions.
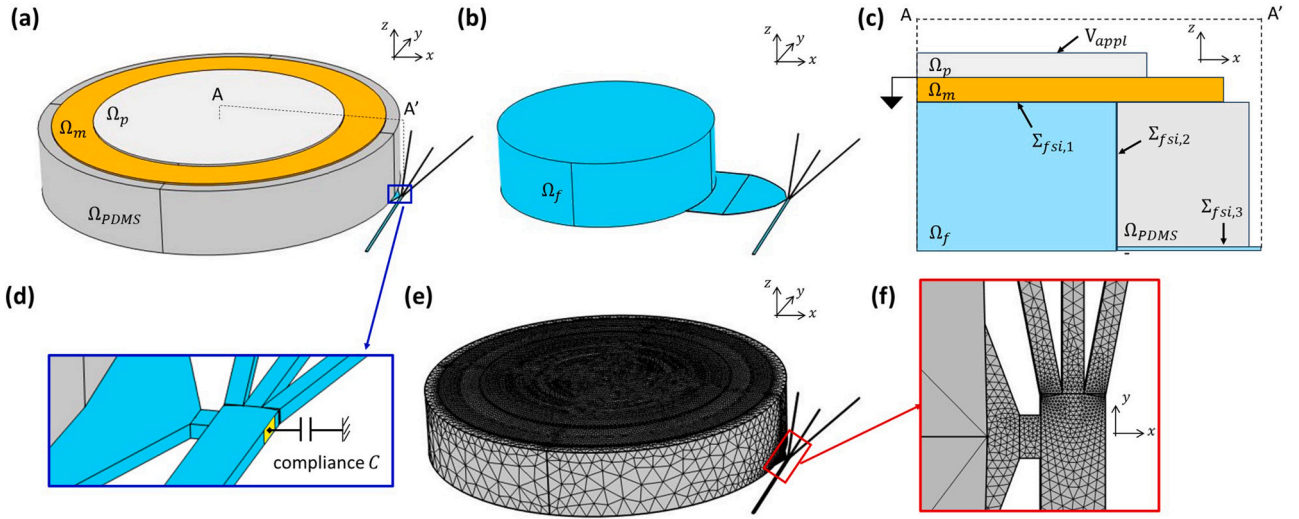

Fig. 2. Geometric model of (a) the whole microfluidic device and (b) the fluid domain only. (c) Schematic representation (not to scale along the z-direction) of the radial section AA', with indication of the different subdomains ($\Omega_p, \Omega_m, \Omega_{PDMS}, \Omega_f$) and the fluid-structure interaction interfaces ($\Sigma_{fsi,1}, \Sigma_{fsi,2}, \Sigma_{fsi,3}$). Applied potential ($V_{appl}$) and electrical ground are also indicated. (d) Zoom showing (in yellow) the fluid boundary Σ_C with associated lumped compliance (which mimics the right oval-shaped lateral chamber present in the experimental device). (e) Typical mesh used in the computation, with (f) zoom of the sorting region.

flow is reached well before the sorting region. To reduce the complexity of the model, the right oval-shaped lateral region and the PDMS above it were modelled as a lumped compliance (cf Fig. 2(d) and Section 3.3), whereas a cylindrical region of PDMS (21.6 mm external diameter) was explicitly modelled below the metal plate.

3.2. Model equations

The displacement field u in the solid domain is governed by the structural equilibrium equations:

$$\rho_s \frac{\partial^2 u}{\partial t^2} = \nabla \bullet T_s + b_s, \text{ in } \Omega_s = \Omega_p \cup \Omega_m \cup \Omega_{PDMS}, \quad (1)$$

where ρ_s is the solid density, T_s is the solid stress tensor, and b_s denotes the body forces (here neglected). In the PZT element, charge conservation law also applies. According to Maxwell's equations in matter, it reads as:

$$\nabla \bullet D = 0, \text{ in } \Omega_p, \quad (2)$$

where D is the electric displacement field.

An isotropic linear elastic constitutive law is considered for the metal substrate and for the PDMS, while the constitutive relations of the PZT element are given by (stress-charge form):

$$T_s = C^E \cdot S - e^t \cdot E, \text{ in } \Omega_p, \quad (3)$$

$$D = e \cdot S + \varepsilon_0 \varepsilon_r^S \cdot E, \text{ in } \Omega_p, \tag{4}$$

where C^E is the elasticity tensor (at constant electric field), e is the tensor of piezoelectric coupling coefficients, ε_0 is the vacuum permittivity, ε_r^S is the tensor of relative electric permittivity (at constant mechanical strain), S is the solid strain tensor:

$$S = \frac{1}{2}\left[\nabla u + (\nabla u)^t\right], \tag{5}$$

and E is the electric field. The latter is related to the electric potential V by $E = -\nabla V$ (under quasi-static approximation).

The velocity field v in the fluid domain obeys the Navier-Stokes equations for momentum balance and mass conservation:

$$\rho_f\left[\frac{\partial v}{\partial t} + (v \bullet \nabla)v\right] = \nabla \bullet T_f + b_f, \text{ in } \Omega_f, \tag{6}$$

$$\rho_f \nabla \bullet v = 0, \text{ in } \Omega_f, \tag{7}$$

where the fluid is assumed to be incompressible with density ρ_f, T_f is the fluid stress tensor, and b_f denotes the body forces (here neglected). A Newtonian constitutive behaviour is assumed for the fluid:

$$T_f = -pI + \mu\left[\nabla v + (\nabla v)^t\right], \text{ in } \Omega_f, \tag{8}$$

where p is the pressure, I is the identity tensor, and μ is the dynamic viscosity.

At the fluid-structure interface ($\Sigma_{fsi} = \Sigma_{fsi,1} \cup \Sigma_{fsi,2} \cup \Sigma_{fsi,3}$, cf Fig. 2 (c)) the following coupling equations hold:

$$v = \frac{\partial u}{\partial t}, \text{ on } \Sigma_{fsi}, \tag{9}$$

$$T_f \bullet n = T_s \bullet n, \text{ on } \Sigma_{fsi}, \tag{10}$$

with n the unit vector normal to the interface.

The values of the material parameters used in the simulations are collected in Table 1 and Table 2.

3.3. Boundary conditions and initial conditions

Boundary conditions are as follows.

- For the PZT element Ω_p (cf also Fig. 2(c)): applied potential V_{appl} on the top boundary, zero potential (ground) on the bottom boundary, zero charge on the lateral boundary, and zero mechanical load on top and lateral boundaries.
- For the metal substrate Ω_m: zero load on lateral and top boundaries (excluding the interface with Ω_p).
- For the PDMS hollow cylinder Ω_{PDMS}: zero displacement on bottom boundaries and zero load elsewhere (excluding the interfaces with Ω_p and Ω_f).
- For the fluid domain Ω_f: a fully developed flow condition at the inlet of the main channel with assigned flow rate Q_{inl}, a null pressure condition at the outlets ($p = 0$ Pa), and a no-slip condition on the device walls.

Table 1
Material parameters.

Material	Density (kg/m^3)	Viscosity (Pa s)	Young's modulus (MPa)	Poisson's ratio
PZT	7500	-	-	-
Metal plate (brass)	8400	-	10^5	0.3
PDMS	970	-	0.75	0.499
Water	1000	0.001	-	-

Table 2
Material properties of PZT.

Parameter	Values
Elasticity tensor C^E (GPa)	$\begin{bmatrix} 127 & 80.2 & 84.7 & 0 & 0 & 0 \\ 80.2 & 127 & 84.7 & 0 & 0 & 0 \\ 84.7 & 84.7 & 117 & 0 & 0 & 0 \\ 0 & 0 & 0 & 29.9 & 0 & 0 \\ 0 & 0 & 0 & 0 & 29.9 & 0 \\ 0 & 0 & 0 & 0 & 0 & 23.5 \end{bmatrix}$
Coupling tensor e (C/m^2)	$\begin{bmatrix} 0 & 0 & 0 & 0 & 17.0345 & 0 \\ 0 & 0 & 0 & 17.0345 & 0 & 0 \\ -6.6228 & -6.6228 & 23.2403 & 0 & 0 & 0 \end{bmatrix}$
Relative permittivity tensor ε_r^S	$\begin{bmatrix} 1704.4 & 0 & 0 \\ 0 & 1704.4 & 0 \\ 0 & 0 & 1433.6 \end{bmatrix}$

- Perfect bonding is assumed on the other internal boundaries.
- Moreover, as shown in Fig. 2(d), a lumped compliance C was modelled at the main channel aperture corresponding to the entrance of the right oval-shaped lateral chamber (Σ_C). The associated equation is:

$$\int_{\Sigma_C} v \bullet n d\Sigma = C \int_{\Sigma_C} \frac{\partial p}{\partial t} d\Sigma. \tag{11}$$

The value of C was numerically estimated. Specifically, a uniform pressure p_{appl} (8 kPa) was applied to the wall of the oval-shaped lateral chamber, and the volume change (ΔVol) associated to the resulting PDMS deformation was quantified (a PDMS block of dimensions 17 mm × 42 mm × 4 mm was considered). The compliance was hence computed as $C = \frac{\Delta Vol}{p_{appl}}$, and turned out to be $C = 4 \times 10^{-13}$ m^3/Pa.

Initial conditions are zero for all variables.

3.4. Model implementation

The model was implemented in COMSOL Multiphysics. The "Solid Mechanics" interface was used for the PZT element Ω_p, the metal substrate Ω_m, and the PDMS hollow cylinder Ω_{PDMS}. As material models, "Piezoelectric Material" was used for Ω_p, while "Linear Elastic Material" was used for Ω_m and for Ω_{PDMS}. In the Ω_p domain, the "Electrostatics" interface was also active, with a "Charge Conservation, Piezoelectric" node. The "Laminar Flow" interface was used for the fluid domain Ω_f. The "Multiphysics" interface was also added to the model, to account for (i) the coupling between the "Solid Mechanics" and "Electrostatics" interfaces within the Ω_p domain, by using the "Piezoelectric Effect" node, and (ii) the coupling between the "Solid Mechanics" and "Laminar Flow" interfaces at the fluid-structure interaction boundaries Σ_{fsi}, by using the "Fluid-Structure Interaction" node with full coupling. The "Explicit event" feature was used to activate the applied voltage.

The finite element mesh (Fig. 2(e, f)) consists of a physics-controlled mesh with unstructured tetrahedral elements. The number of elements and the number of degrees of freedom typically considered were about 1.2 million and 2.4 million, respectively. Mechanical, electrical, and fluidic problems are fully coupled, and a segregated solver is used. To improve problem conditioning, the flowing units were used for the fundamental quantities: length in mm, time in ms, mass in mg, and charge in μC. The computational time on a workstation with dual Intel (R) Xeon(R) CPU Gold 6226 R @ 2.89 GHz and 256 GB RAM was about 7 h, for each numerical test.

3.5. Central streamline analysis

To quantify the fluid flow displacement caused by the PZT actuation we analysed the behaviour of the streamline that originates at the central point of the main channel entrance (Fig. 3(a)). For each simulation time, we extracted the streamline coordinates and fitted a linear model to the projection on the xy-plane of the streamline portion falling in the
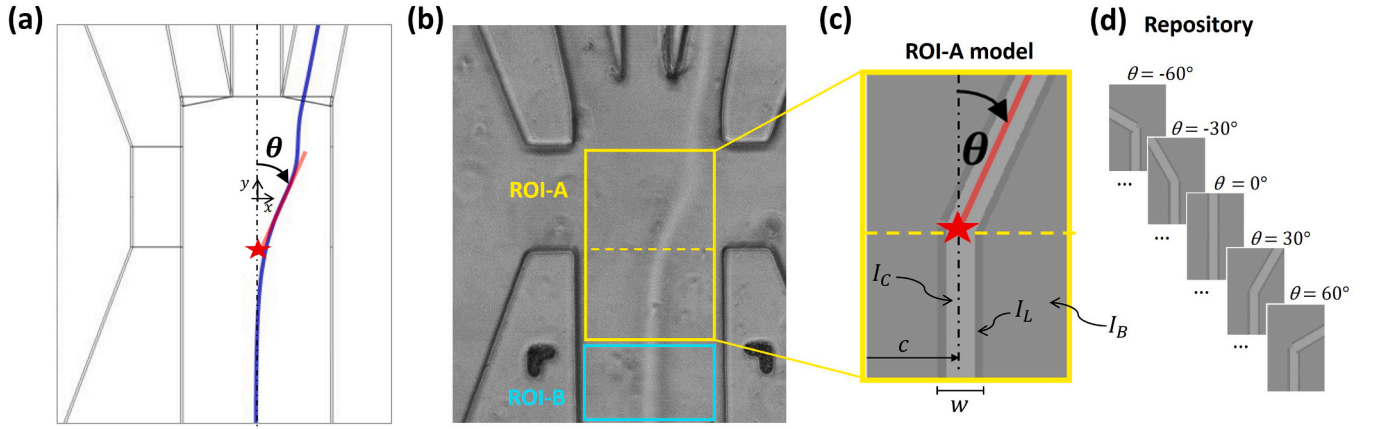
Fig. 3. (a) Linear fit of the simulated central streamline, with indication of the rotation angle θ. (b)-(d) Image-based quantification of the experimental central stream rotation. (b) Exemplary microscopy snapshot of the sorting region (the sample stream is deflected towards the right collection channel). The regions-of-interest ROI-A and ROI-B are highlighted. (c) Model of ROI-A, with indication of the angle θ and the relevant model parameters (see text for details). (d) Five examples from the repository ($\theta = -60°, -30°, 0, 30°, 60°$).

sorting region:

$$y = c_1 x + c_0, \qquad (12)$$

where c_1 is the fitted parameter and c_0 is set to impose the passage of the model through point $(0 \mu m, -50 \mu m)$, shown as a star in Fig. 3(a). The deflection of the streamline with respect to the main channel axis was accordingly quantified by the rotation angle $\theta = \text{atan}(c_1)$.

4. Image-based approach for experimental device characterization

To experimentally quantify the deflection of the sample stream induced by the piezoelectric actuator we designed an original image-based approach, described in the following. The method was implemented in MATLAB.

Fig. 3(b) shows an exemplary image frame. The sample stream is distinguishable from the sheath flows since it is lighter. Moreover, the two interfaces between the sample and the sheath flows appear as two darker bands. Two regions of interest (ROIs) are highlighted in the image frame, referred to as ROI-A (sorting region) and ROI-B (pre-sorting region). During piezoelectric actuation, ROI-B does not change across the different video frames. On the other hand, ROI-A captures the sample stream displacement. Aiming at simple and robust image-processing, we created a model image of ROI-A (Fig. 3(c)) with only one degree of freedom that is the stream deflection angle θ. The other geometric parameters of the model image, namely the sample stream centre location c and the sample stream width w, are measured in ROI-B from the first frame of each video. In order to increase robustness with respect to noise, the average row of ROI-B is computed, from which w and c are automatically extracted. The intensity levels of the different parts of the model image - namely those of the central stream (I_C), the lateral bands (I_L), and the background (I_B) - are manually extracted from ROI-A of the first frame of each video. The width of each darker lateral band is estimated as $w/6$.

For each video, a model repository of ROI-A corresponding to 65 equispaced values of θ in the range $[-60°, 60°]$ was generated (Fig. 3(d)). The acquired ROI-A of each video frame was then matched with the closest model from the repository (i.e., minimum norm of difference image) and was assigned the corresponding value of θ.

5. Results and discussion

5.1. Numerical characterization results

In all numerical tests, a set-up period of duration $T_i = 250$ s at zero applied potential is considered, to achieve a steady-state condition. The inlet flow rate increases linearly from $Q_{inl} = 0$ μl/min at $t = 0$ to $Q_{inl} = 20$ μl/min at $t = T_i/2$, and is kept constant at 20 μl/min for $t > T_i/2$. The value of 20 μl/min was chosen to mimic the experimental conditions (5 μl/min sample flow and 15 μl/min sheath flow).

The simulation results relevant to the set-up period ($0 \le t \le T_i$) are shown in Fig. 4. While approaching the steady state, the pressure in the sorting region increases. Accordingly, the PDMS, the metal plate, and the PZT element are displaced outwards. Therefore, part of the inlet flow rate is accommodated into the lumped compliance and the cylindrical chamber (cf streamlines in Fig. 4(b, c)). The upward displacement of the metal plate reaches about 40 μm (mean displacement) at $t = T_i$. The amount of flow diverted from the main channel progressively decreases while the overall outlet flow rate Q_{out} progressively approaches Q_{inl}. The repartition of the flow rate among the three outlet channels is governed by their hydraulic resistance, which in turn is proportional to their lengths ($L_1 = 7.5$ mm, $L_2 = L_3 = 10$ mm). Accordingly, $Q_2/Q_1 = Q_3/Q_1 = 3/4$, where Q_i denotes the flow rate through outlet O_i and $Q_1 + Q_2 + Q_3 = Q_{out}$.

At $t = T_i$, either a sinusoidal actuation or a pulse actuation is activated. The sinusoidal actuation case is reported in Fig. 5. An applied potential at 3 Hz frequency and 5, 7.5, or 10 V_{pp} amplitude is considered. Ten cycles are simulated (to ease convergence, the voltage amplitude reaches its full value at the end of the second cycle). The vertical displacement of the metal plate, u_z, follows the behaviour of the applied potential V_{appl}, namely, a positive voltage induces an upward displacement. The overall outlet flow rate is accordingly in counter-phase with V_{appl}. A substantial proportionality with respect to the amplitude of the applied voltage is found in the tested range. The peak-to-peak amplitudes of the oscillation of the vertical displacement u_z are 1.53 μm, 1.14 μm, and 0.764 μm, respectively at 10, 7.5, and 5 V_{pp}, whereas the peak-to-peak amplitudes of the oscillation of the overall outlet flow rate are 0.186 μl/min, 0.139 μl/min, and 0.0923 μl/min. Three exemplary streamline paths - corresponding to deflection to the right, unperturbed case, and deflection to the left - are shown in Fig. 5(b). It can be noticed that in the right-deflection case the streamlines arriving from the right portion of the main channel move toward the boundary Σ_C, where the lumped compliance is applied, mimicking the deformability of the right oval-shaped lateral chamber (cf Section 3.3).
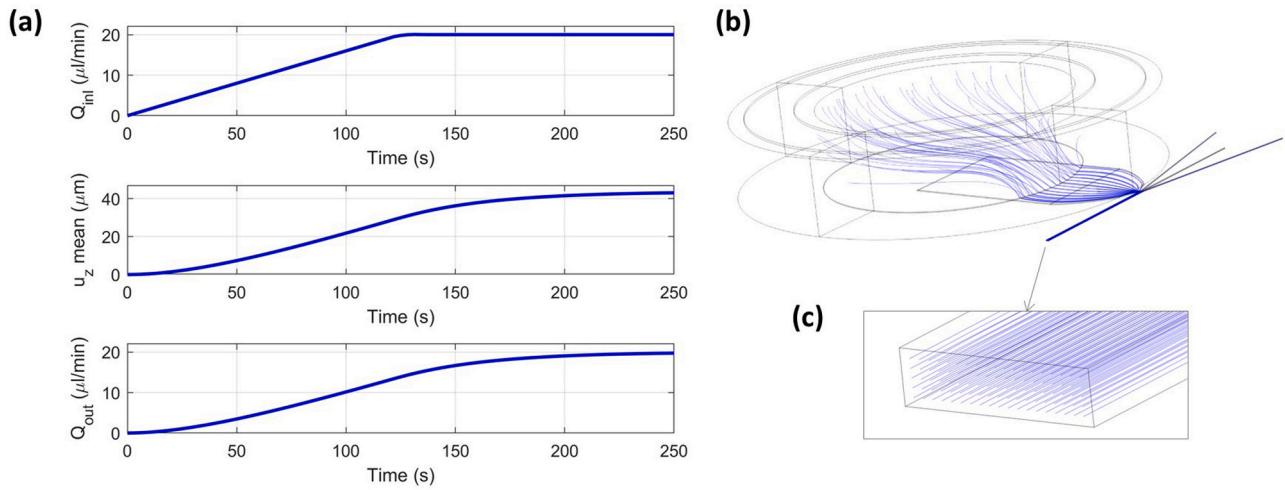
Fig. 4. Numerical characterization, set-up period ($0 \le t \le T_i$). (a) From top to bottom: inlet flow rate (Q_{inl}), average over $\Sigma_{fsi,1}$ of the vertical displacement of the metal plate (u_z), and overall outlet flow rate ($Q_{out} = Q_1 + Q_2 + Q_3$). (b) Visualization of the streamlines originating at the inlet section (cf zoom in panel (c)), at first time step (i.e., $t = 5$ ms).
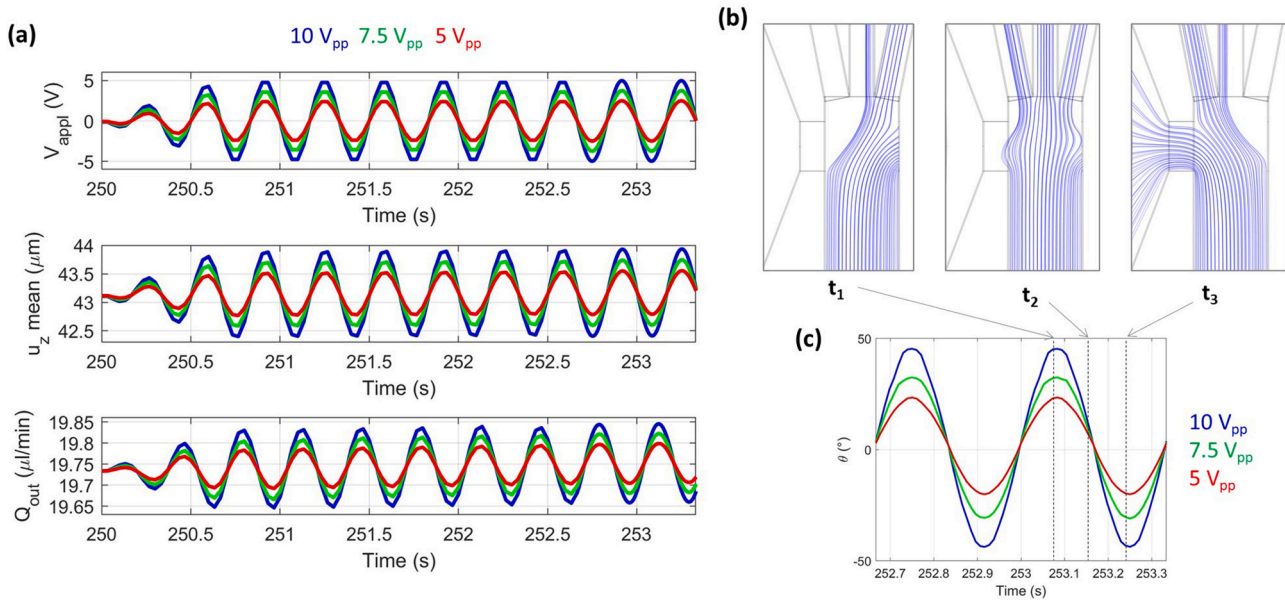

Fig. 5. Numerical characterization, sinusoidal drive signal (10 cycles, reaching max amplitude at the end of second cycle). (a) From top to bottom: applied potential V_{appl} (3 Hz, 5, 7.5, or 10 V_{pp}), average over $\Sigma_{fsi,1}$ of the vertical displacement of the metal plate (u_z), and overall outlet flow rate ($Q_{out} = Q_1 + Q_2 + Q_3$). (b) Path of the streamlines originating at the main channel inlet, at three relevant time instants of the last stimulation cycle (10 V_{pp} case): t_1 ($V_{appl} = -5$ V), t_2 ($V_{appl} = 0$ V), and t_3 ($V_{appl} = 5$ V). (c) Rotation angle of the central streamline (last 2 cycles).

The time behaviour of the rotation angle θ of the central streamline (cf Section 3.5) is shown in Fig. 5(c). It is a sinusoidal waveform in counterphase with the applied voltage and approximately proportional to its amplitude. Specifically, the amplitude of θ turned out to be 45.4°, 32.5°, and 23.4°, respectively at 10, 7.5, and 5 V_{pp}.

Fig. 6 reports the results relevant to the pulse drive signal. A single pulse of 20 ms duration and 3 V amplitude is considered, followed by a final phase (50 ms) at zero applied potential. Like the sinusoidal case, the vertical displacement of the metal plate closely follows the behaviour of the applied potential, with a negative pulse of 3 V amplitude inducing a 0.45 μm drop of u_z. The pressure at the interface between the fluid and the metal plate ($\Sigma_{fsi,1}$) correspondingly increases of about 0.1 kPa (with respect to a pre-pulse value of 7.31 kPa). A pressure increase is also found at the sorting region, as well as streamlines deflection towards the right outlet and the lumped compliance (Fig. 6(b)). At the

central time of the pulse, the rotation angle of the central streamline is $\theta = 23°$.

5.2. Experimental characterization results

For the experimental characterization of the actuator, we monitored the rotation angle θ of the sample stream by using the image-processing approach described in Section 4. In case of sinusoidal drive signal, applied voltage (10 V_{pp}) at frequencies from 3 Hz to 1 kHz were tested. The resulting rotation θ of the sample stream exhibited a sinusoidal time course. A slight offset (i.e., a non-null baseline value) was present. Fig. 7 (a) shows the raw rotation angle returned by the image-processing routine (thick blue curve). In the video recorded at 50 Hz stimulation frequency, for small sample stream deflection, the contrast between the sample stream and the sheath flows was quite low, resulting in image
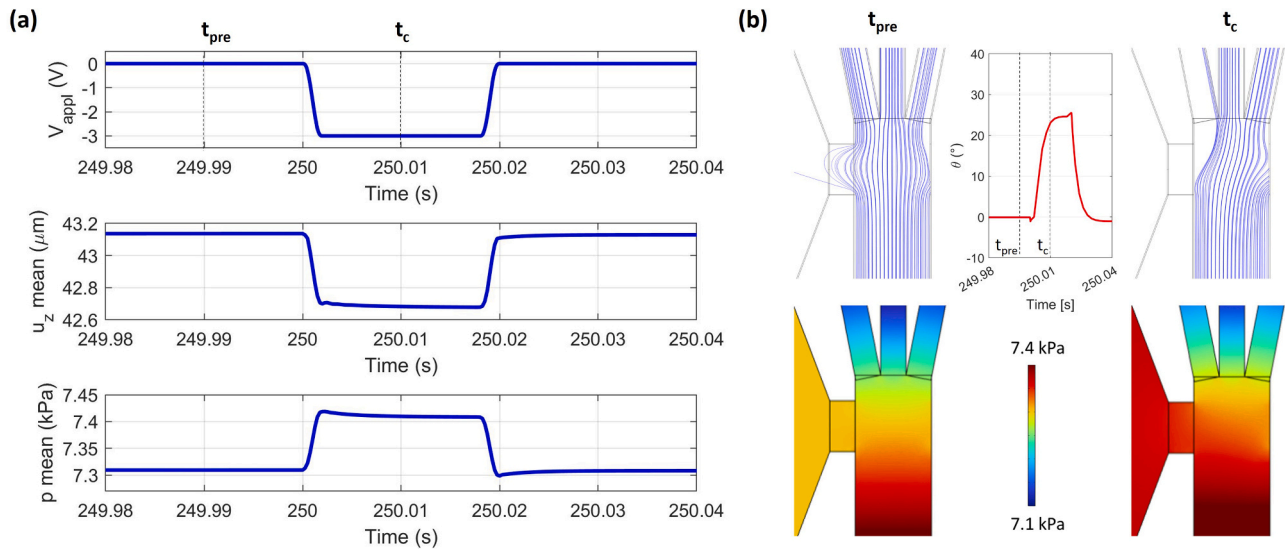
Fig. 6. Numerical characterization, pulse drive signal. (a) From top to bottom: applied potential V_{appl} (-3 V pulse, 20 ms duration, 2 ms rise and fall times), average over $\Sigma_{fsi,1}$ of the vertical displacement of the metal plate (u_z) and of the pressure p. (b) Path of the streamlines originating at the main channel inlet (top row) and pressure distribution (bottom row), at two relevant times: before pulse actuation (t_{pre}) and at the central time of the pulse (t_c). The time plot of the rotation angle of the central streamline is also reported.
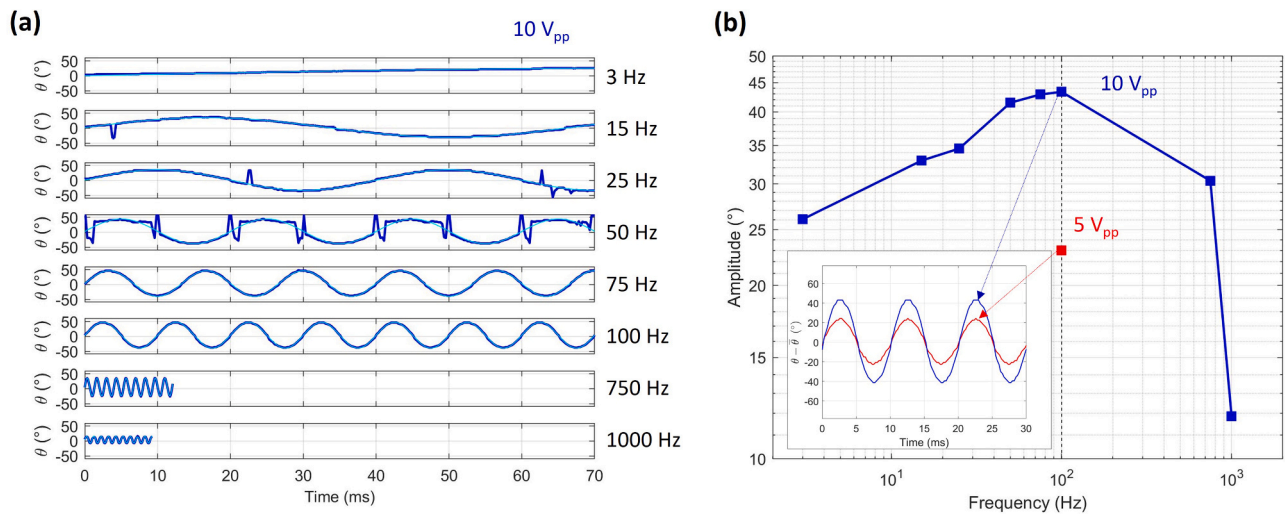

Fig. 7. Experimental characterization, sinusoidal drive signal. (a) Rotation angle of the sample stream $\theta(t)$ for drive signals (10 V_{pp}) at (from top to bottom) 3, 15, 25, 50, 75, 100, 500, and 1000 Hz. Raw data (blue); fitted sinusoids (cyan). (b) Bode diagram (amplitude plot). At 100 Hz, 5 V_{pp} voltage is also considered (red square). Inset: rotation angle at 10 V_{pp} (blue) and 5 V_{pp} (red). The baseline value $\bar{\theta}$ has been subtracted from $\theta(t)$ to ease amplitude comparison.

processing artefacts. A sinusoidal fit of the raw rotation angle is also reported in Fig. 7(a) (thin cyan curve, fit model: $A\sin(2\pi f + \varphi) + B$). The fitting procedure allowed to manage possible processing artifacts and to verify that the rotation frequency f was the same as the frequency of the applied voltage. The Bode amplitude plot is reported in Fig. 7(b). The rotation amplitude A increases from 26° at 3 Hz to 43.3° at 100 Hz and drops to 11.8° at 1 kHz, due to the inertia of the overall mechanical system. In the inset, for the 100 Hz case, the time course of θ at 10 V_{pp} is compared to that at 5 V_{pp}, which exhibits a rotation amplitude of 22.9°. An exemplary video of the sinusoidal actuation case is provided as supplementary material (Video S1, described in Section 3 of the Supplementary Material file).

In case of pulse drive signal, pulses of duration T_{on} ranging from 20 ms to 0.5 ms were tested, at 5 V or 3 V pulse amplitude. In each test, a train of pulses were administrated with repetition period T. The time course of the resulting sample rotation θ is reported in Fig. 8(a). The individual pulses do not interfere with each other. For T_{on} of 20, 10, or

5 ms, the rotation $\theta(t)$ follows the time course of the applied voltage. Slight overshoots are found at pulse activation/deactivation, and the value of theta slightly decreases during the pulse-on phase. The value of θ at half pulse duration (θ_c) is reported in Table 3. For T_{on} of 1 or 0.5 ms, the rise phase of $\theta(t)$ is not complete when the fall phase begins. In those cases, the maximum rotation (θ_{max}) is reported in Table 3. In all cases, the rotation is larger at 5 V than at 3 V. Finally, we performed a test (at 20 ms pulse duration) with inverted pulse polarity and found a symmetric response of the system (Fig. 8(b)). An exemplary video of the pulse actuation case is provided as supplementary material (Video S2, described in Section 3 of the Supplementary Material file).

6. Discussion and conclusions

We introduced an approach for the design and characterization of a microfluidic piezoelectric sorter. The approach hinges on two tools: a finite element model for *in-silico* analysis of device functioning and an
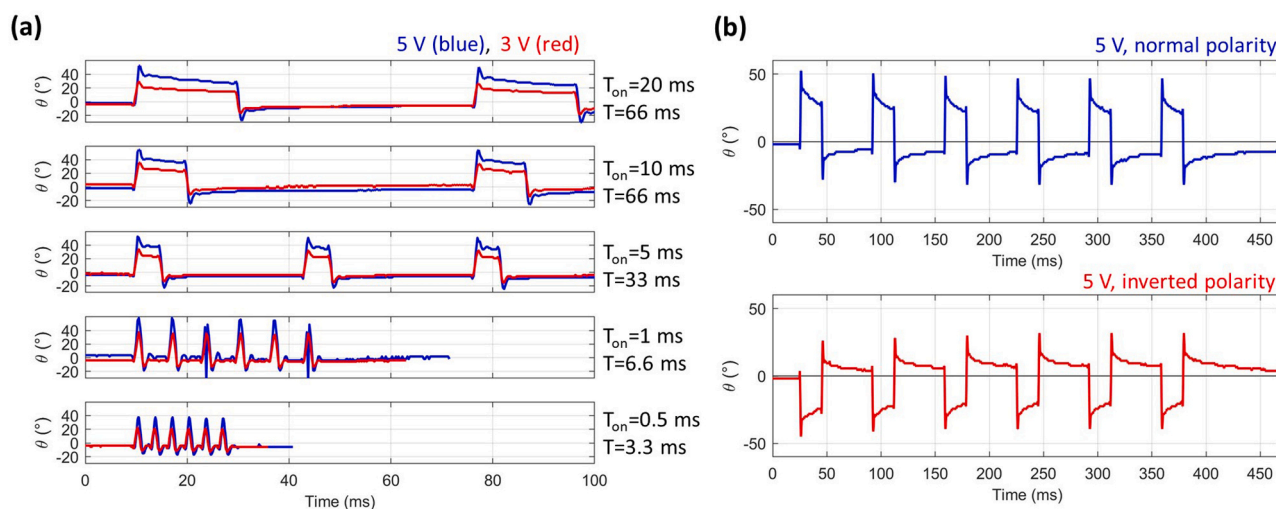
Fig. 8. Experimental characterization, pulse drive signal. (a) Rotation angle of the sample stream $\theta(t)$. From top to bottom, T_{on} = 20, 10, 5, 1, and 0.5 ms. Pulse amplitude is 5 V (blue) or 3 V (red). (b) Comparison of pulse drive signal with normal polarity (i.e., V_{on} = 2.5, V_{off} = − 2.5) and inverted polarity (i.e., V_{on} = − 2.5, V_{off} = 2.5).

Table 3
Experimental sample stream rotation in case of pulse drive signal (θ_c, rotation angle at half pulse duration; θ_{max} maximum rotation angle).

Pulse amplitude	T_{on} = 20 ms	T_{on} = 10 ms	T_{on} = 5 ms	T_{on} = 1 ms	T_{on} = 0.5 ms
5 V	θ_c = 32°	θ_c = 39°	θ_c = 39°	θ_{max} = 58°	θ_{max} = 37°
3 V	θ_c = 17°	θ_c = 24°	θ_c = 24°	θ_{max} = 37°	θ_{max} = 22°

image-based strategy for experimental monitoring of flow deflection.

The numerical model of the microfluidic system was able to mimic the main features of the actual device. To obtain this result, it was critical to include the deformability of the PDMS in the model. In a microfluidic device with rigid walls, the streamlines would not enter the right oval-shaped lateral chamber due to fluid incompressibility, and the rotation of the central streamline would be asymmetrical (rotations to the left larger than rotations to the right). Furthermore, as shown in Sections 1 and 2 of the Supplementary Material, the implementation of a fully coupled fluid-structure interaction turned out to be essential to reproduce in simulation the sinusoidal oscillation manifested by the experimental sample stream under sinusoidal actuation (Fig. S1, Fig. S2). In case of pulse actuation, the experimental results exhibit a sharp rise followed by a slow decay, not appearing in simulation (Fig. S3). The difference between simulation and experiments may be partially explained by the pulse-voltage smoothing (2 ms rise and fall times) introduced in simulation to ease convergence. Moreover, calibration of model parameters (e.g., PDMS Young's modulus) may bring the simulation results closer to the experimental ones.

The numerical model also provided insights on quantities that are not straightforward to monitor experimentally, such as the deflection of the metal plate and the pressure acting upon it, and the behaviour of the streamlines inside the cylindrical chamber. However, the 3D and multiphysics nature of the numerical model required care to facilitate convergence. Specifically, we reduced model complexity by substituting the right oval-shaped chamber with a lumped compliance, and we used a tailored scaling to improve conditioning.

Comparable voltages (a few volts) were needed to achieve effective fluid deflection (tens of degrees) numerically and experimentally. In both cases, fluid displacement was approximately proportional to the intensity of the applied voltage.

The numerical and the experimental characterization of the sample stream deflection share a common approach. They both consider a linear approximation of the deflected streamlines in the sorting region, quantified by means of a rotation angle θ. This is a simple and effective way to

monitor the time course of the fluid response. By geometric arguments, a cell focused along the microchannel axis would be unsorted for $|\theta| \leq 9.5°$ or left/right sorted for $9.5° < |\theta| < 26.6°$ (left for negative values, right for positive values). For θ magnitude higher than 26.6° the cell could be deflected towards the left or the right oval-shaped chambers (according to the sign of θ). A real-time implementation of the image-based approach could be used to detect this situation and accordingly reduce the applied voltage, thus directing the sample flow towards the outlet channels.

The image processing approach turned to be quite effective. The adaptive selection of the model parameters (c, w, I_C, I_L, I_B) ensures that the strategy is robust with respect to slight off-centering of the sample stream and variations of the illumination settings across different videos. The use of only one degree of freedom θ results in a small repository from which the best fit model is rapidly identified. Accordingly, the approach has potential for real-time implementation.

As a perspective, the numerical model could be adapted to other device geometries or enriched by introducing particle tracing. From the experimental point of view, an impedance sensor will be integrated into the device to drive the piezoelectric actuator based on the electrical phenotype of target cells.

CRediT authorship contribution statement

Brandi Cristian: Writing – original draft, Software, Investigation, Formal analysis. **De Ninno Adele:** Resources, Methodology, Investigation, Funding acquisition, Conceptualization. **Verona Enrico:** Methodology. **Businaro Luca:** Methodology. **Bisegna Paolo:** Writing – review & editing, Software, Resources, Methodology. **Caselli Federica:** Writing – original draft, Software, Resources, Methodology, Investigation, Funding acquisition, Formal analysis, Conceptualization.

Declaration of Competing Interest

The authors declare that they have no known competing financial

interests or personal relationships that could have appeared to influence the work reported in this paper.

Data availability

Data will be made available on request.

Acknowledgments

Appendix A. Supporting information

Supplementary data associated with this article can be found in the online version at doi:10.1016/j.sna.2024.115074.

References

[1] C. Wyatt Shields IV, C.D. Reyes, G.P. López, Microfluidic cell sorting: a review of the advances in the separation of cells from debulking to rare cell isolation, Lab Chip 15 (2015) 1230–1249, https://doi.org/10.1039/C4LC01246A.

[2] Y. Shen, Y. Yalikun, Y. Tanaka, Recent advances in microfluidic cell sorting systems, Sens Actuators B Chem. 282 (2019) 268–281, https://doi.org/10.1016/j.snb.2018.11.025.

[3] R. Nasiri, A. Shamloo, S. Ahadian, L. Amirifar, J. Akbari, M.J. Goudie, K.J. Lee, N. Ashammakhi, M.R. Dokmeci, D. Di Carlo, A. Khademhosseini, Microfluidic-based approaches in targeted cell/particle separation based on physical properties: fundamentals and applications, Small 16 (2020) 2000171, https://doi.org/10.1002/smll.202000171.

[4] N. Lu, H.M. Tay, C. Petchakup, L. He, L. Gong, K.K. Maw, S.Y. Leong, W.W. Lok, H. B. Ong, R. Guo, K.H.H. Li, H.W. Hou, Label-free microfluidic cell sorting and detection for rapid blood analysis, Lab Chip 23 (2023) 1226–1257, https://doi.org/10.1039/d2lc00904h.

[5] W. Geng, Y. Liu, N. Yu, X. Qiao, M. Ji, Y. Niu, L. Niu, W. Fu, H. Zhang, K. Bi, X. Chou, An ultra-compact acoustofluidic device based on the narrow-path travelling surface acoustic wave (np-TSAW) for label-free isolation of living circulating tumor cells, Anal. Chim. Acta 1255 (2023) 341138, https://doi.org/10.1016/j.aca.2023.341138.

[6] L. Jiang, F. Liang, M. Huo, M. Ju, J. Xu, S. Ju, L. Jin, B. Shen, Study on three-dimensional dielectrophoresis microfluidic chip for separation and enrichment of circulating tumor cells, Micro Eng. 282 (2023) 112100, https://doi.org/10.1016/j.mee.2023.112100.

[7] C.H. Chen, S.H. Cho, F. Tsai, A. Erten, Y.H. Lo, Microfluidic cell sorter with integrated piezoelectric actuator, Biomed. Micro 11 (2009) 1223–1231, https://doi.org/10.1007/s10544-009-9341-5.

[8] Z. Cheng, X. Wu, J. Cheng, P. Liu, Microfluidic fluorescence-activated cell sorting (μFACS) chip with integrated piezoelectric actuators for low-cost mammalian cell enrichment, Microfluid Nanofluidics 21 (2017) 9, https://doi.org/10.1007/s10404-017-1847-1.

[9] L. Schmid, D.A. Weitz, T. Franke, Sorting drops and cells with acoustics: acoustic microfluidic fluorescence-activated cell sorter, Lab Chip 14 (2014) 3710–3718, https://doi.org/10.1039/c4lc00588k.

[10] C. Honrado, P. Bisegna, N.S. Swami, F. Caselli, Single-cell microfluidic impedance cytometry: from raw signals to cell phenotypes using data analytics, Lab Chip 21 (2021) 22–54, https://doi.org/10.1039/D0LC00840K.

[11] Y. Ai, P. Li, Label-free multivariate biophysical phenotyping-activated acoustic sorting at the single-cell level, Anal. Chem. 93 (2021) 4108–4117, https://doi.org/10.1021/acs.analchem.0c05352.

[12] A. Salahi, C. Honrado, A. Rane, F. Caselli, N.S. Swami, Modified red blood cells as multimodal standards for benchmarking single-cell cytometry and separation based on electrical physiology, Anal. Chem. 94 (2022) 2865–2872, https://doi.org/10.1021/acs.analchem.1c04739.

[13] H. Daguerre, M. Solsona, J. Cottet, M. Gauthier, P. Renaud, A. Bolopion, Positional dependence of particles and cells in microfluidic electrical impedance flow cytometry: origin, challenges and opportunities, Lab Chip 20 (2020) 3665–3689, https://doi.org/10.1039/d0lc00616e.

[14] J. Zhong, M. Liang, Q. Tang, Y. Ai, Selectable encapsulated cell quantity in droplets via label-free electrical screening and impedance-activated sorting, Mater. Today Bio 19 (2023) 100594, https://doi.org/10.1016/j.mtbio.2023.100594.

[15] B. de Wagenaar, S. Dekker, H.L. de Boer, J.G. Bomer, W. Olthuis, A. Van Den Berg, L.I. Segerink, Towards microfluidic sperm refinement: impedance-based analysis and sorting of sperm cells, Lab Chip 16 (2016) 1514–1522, https://doi.org/10.1039/C6LC00256K.

[16] X. Qi, D.M. Carberry, C. Cai, S. Hu, Z. Yuan, H. Rubinsztein-Dunlop, J. Guo, Optical sorting and cultivation of denitrifying anaerobic methane oxidation archaea, Biomed. Opt. Express 8 (2017) 934, https://doi.org/10.1364/boe.8.000934.

[17] J. Zhao, Z. You, Spark-generated microbubble cell sorter for microfluidic flow cytometry, Cytom. Part A 93 (2018) 222–231, https://doi.org/10.1002/cyto.a.23296.

[18] L. Gong, C. Petchakup, H.W. Hou, Integrated Label-Free Microfluidic Platform for Automated Cellular Monitoring and Real-Time Actuated Sorting of Cell-Laden Microcarriers, in: MicroTAS 2021 - 25th International Conference on Miniaturized Systems for Chemistry and Life Sciences, 2021.

[19] M. Matsumoto, S. Tashiro, T. Ito, K. Takahashi, G. Hashimoto, J. Kajihara, Y. Miyahara, H. Shiku, Y. Katsumoto, Fully closed cell sorter for immune cell therapy manufacturing, Mol. Ther. Methods Clin. Dev. 30 (2023) 367–376, https://doi.org/10.1016/j.omtm.2023.07.012.

[20] X. Chen, Y. Gu, J. Chen, C.H. Lee, I. Gagne, R. Tang, L. Waller, Z. Zhang, A. C. Zhang, Y. Han, W. Wang, I.Y. Lian, S.H. Cho, Y.H. Lo, Image-guided cell sorting using fast scanning lasers, APL Photonics 5 (2020) 040801, https://doi.org/10.1063/1.5144117.

[21] C.H. Chen, S.H. Cho, H.I. Chiang, F. Tsai, K. Zhang, Y.H. Lo, Specific sorting of single bacterial cells with microfabricated fluorescence-activated cell sorting and tyramide signal amplification fluorescence in situ hybridization, Anal. Chem. 83 (2011) 7269–7275, https://doi.org/10.1021/ac2013465.

[22] Y. Zhao, A.S. Abdelfattah, Y. Zhao, A. Ruangkittisakul, K. Ballanyi, R.E. Campbell, D.J. Harrison, Microfluidic cell sorter-aided directed evolution of a protein-based calcium ion indicator with an inverted fluorescent response, Integr. Biol. (U. Kingd.) 6 (2014) 714–725, https://doi.org/10.1039/c4ib00039k.

[23] S. Sakuma, Y. Kasai, T. Hayakawa, F. Arai, On-chip cell sorting by high-speed local-flow control using dual membrane pumps, Lab Chip 17 (2017) 2760–2767, https://doi.org/10.1039/c7lc00536a.

[24] K. Cai, S. Mankar, A. Maslova, T. Ajiri, T. Yotoriyama, Amplified piezoelectrically actuated on-chip flow switching for a rapid and stable microfluidic fluorescence activated cell sorter, RSC Adv. 10 (2020) 40395–40405, https://doi.org/10.1039/d0ra04919k.

[25] J. Shemesh, A. Bransky, M. Khoury, S. Levenberg, Advanced microfluidic droplet manipulation based on piezoelectric actuation, Biomed. Micro 12 (2010) 907–914, https://doi.org/10.1007/s10544-010-9445-y.

[26] S. Krishnamoorthy, A.S. Bedekar, J.J. Feng, S. Sundaram, Need for simulation-based design analysis and optimization, JALA: J. Assoc. Lab. Autom. 11 (2006) 118–127, https://doi.org/10.1016/j.jala.2006.02.007.

[27] V. Carvalho, R.O. Rodrigues, R.A. Lima, S. Teixeira, Computational simulations in advanced microfluidic devices: a review, Micromachines 12 (2021) 1149, https://doi.org/10.3390/mi12101149.

[28] P. Bisegna, F. Caselli, S. Marfia, E. Sacco, A new SMA shell element based on the corotational formulation, Comput. Mech. 54 (2014) 1315–1329, https://doi.org/10.1007/s00466-014-1061-x.

[29] F. Caselli, P. Bisegna, Simulation and performance analysis of a novel high-accuracy sheathless microfluidic impedance cytometer with coplanar electrode layout, Med Eng. Phys. 48 (2017) 81–89, https://doi.org/10.1016/j.medengphy.2017.04.005.

[30] M. Bu, T. Melvin, G. Ensell, J.S. Wilkinson, A.G.R. Evans, Design and theoretical evaluation of a novel microfluidic device to be used for PCR, J. Micromech. Microeng. 13 (2003) S125, https://doi.org/10.1088/0960-1317/13/4/321.

[31] T. Ma, S. Sun, B. Li, J. Chu, Piezoelectric peristaltic micropump integrated on a microfluidic chip, Sens Actuators A Phys 292 (2019) 90–96, https://doi.org/10.1016/j.sna.2019.04.005.

[32] J.E. Rojas, J.J., Morale, Design and Simulation of a Piezoelectric Actuated Valveless Micropump, in: Proceedings of the COMSOL Conference 2015, Boston, MA, 2015.

[33] J.B. Holman, X. Zhu, H. Cheng, Piezoelectric micropump with integrated elastomeric check valves: design, performance characterization and primary application for 3D cell culture, Biomed. Micro. 25 (2023) 5, https://doi.org/10.1007/s10544-022-00645-9.

[34] S.A.F.F. Yazdi, A. Corigliano, R. Ardito, 3-D design and simulation of a piezoelectric micropump, Micromachines 10 (2019) 259, https://doi.org/10.3390/mi10040259.

[35] H. Shimizu, Y. Uetsuji, Fluid-structure and electric coupled analysis of a valveless microfluidic system with metal-capped piezoelectric actuator, Sens Actuators A Phys. 333 (2022) 113232, https://doi.org/10.1016/j.sna.2021.113232.

[36] X. Wang, J. Zheng, M.A. Iyer, A.H. Szmelter, D.T. Eddington, S.S.Y. Lee, Spatially selective cell treatment and collection for integrative drug testing using hydrodynamic flow focusing and shifting, PLoS One 18 (2023) e0279102, https://doi.org/10.1371/journal.pone.0279102.

[37] G. Choi, R. Nouri, L. Zarzar, W. Guan, Microfluidic deformability-activated sorting of single particles, Micro Nanoeng. 6 (2020) 11, https://doi.org/10.1038/s41378-019-0107-9.

[38] W. Wu, J. Wu, J.H. Kim, N.Y. Lee, Instantaneous room temperature bonding of a wide range of non-silicon substrates with poly(dimethylsiloxane) (PDMS) elastomer mediated by a mercaptosilane, Lab Chip 15 (2015) 2819–2825, https://doi.org/10.1039/c5lc00285k.

[39] F. Caselli, A. De Ninno, R. Reale, L. Businaro, P. Bisegna, A Bayesian approach for coincidence resolution in microfluidic impedance cytometry, IEEE Trans. Biomed. Eng. 68 (2020) 340–349, https://doi.org/10.1109/TBME.2020.2995364.

[40] R. Reale, A. De Ninno, L. Businaro, P. Bisegna, F. Caselli, Electrical measurement of cross - sectional position of particles flowing through a microchannel, Microfluid Nanofluidics 22 (2018) 41, https://doi.org/10.1007/s10404-018-2055-3.

[41] T.L. Bergman, A.S. Lavine, F.P. Incropera, D.P. Dewitt, Fundamentals of heat and mass transfer, Fundam. Heat. Mass Transf. 7th Ed. (2011).

Cristian Brandi received his Master of Science in Biomedical Engineering in 2022. Currently he is a Contract Researcher at the University of Rome Tor Vergata. His research interests include the numerical and experimental characterization of microfluidic systems for single-cell analysis and manipulation.

Luca Businaro is a micro and nanofabrication scientist at Institute for Photonics and Nanotechnologies, part of the Italian National Research Council. His primary scientific interest dwells in reconstituting on microfluidic chips complex biological systems such as the insult-immune system interface.

Adele De Ninno is a Researcher at the Italian National Research Council, Institute for Photonics and Nanotechnologies. Her research interests include microfluidics-based approaches for mimicking complex biological processes, organs-on-chip and lab-on-a-chip devices for point-of-care diagnostic applications.

Paolo Bisegna serves as Professor of Mechanics of Materials and Structures and as Director of the Structural Engineering Doctoral Program at the University of Rome Tor Vergata. His research interests include biomedical microdevices, biomechanics and metamaterials.

Enrico Verona Has been Research Director at the "O. M. Corbino" Institute of Acoustics of the Italian National Research Council (CNR) and Director of the Institute. Presently he is Associate Senior Researcher at the Institute for Photonics and Nanotechnologies of CNR. His research interests include physical acoustics, SAW and BAW propagation and their applications to electroacoustic devices and sensors.

Federica Caselli is Associate Professor of Biomedical Engineering at University of Rome Tor Vergata. Her research interests include the development of microfluidic devices for biomedical applications, with a special focus on impedance-based single-cell biophysical phenotyping.

Supplementary Material to:

Numerical and experimental characterization of a piezoelectric actuator for microfluidic cell sorting

Cristian Brandi,[a,§] Adele De Ninno,[b,§] Enrico Verona,[b] Luca Businaro,[b] Paolo Bisegna,[a] Federica Caselli[a,*]

[a]Department of Civil Engineering and Computer Science, University of Rome Tor Vergata, Rome, Italy
[b]Institute for Photonics and Nanotechnology, Italian National Research Council, Rome, Italy
(§, equal contribution; *, corresponding author)

1. Comparison of different fluid-structure coupling modalities

In this supplementary section we compare the simulation results obtained with three different fluid-structure coupling modalities. They are: (i) 'Fully coupled' (as in the main text); (ii) 'One-way' coupling; (iii) 'Hybrid' coupling (see table below for the relevant settings).

Label	Metal plate-fluid interface ($\Sigma_{fsi,1}$)	PDMS-fluid interface ($\Sigma_{fsi,2}, \Sigma_{fsi,3}$)
'Fully coupled'	velocity transmission to fluid and fluid loading on structure	velocity transmission to fluid and fluid loading on structure
'One-way'	velocity transmission to fluid	velocity transmission to fluid
'Hybrid'	velocity transmission to fluid	velocity transmission to fluid and fluid loading on structure

As case study, we considered the sinusoidal actuation at 10 V_{pp} and 3 Hz. The rotation angle θ of the central streamline obtained with the different approaches are collected in **Figure S1**. As shown in the figure, the 'One-way' coupling approach (green curve) shows a saturation of the streamline rotation angle θ to the extremal values ($\theta = \pm 90°$). As a matter of fact, in the 'One-way' approach the hollow PDMS cylinder does not deform significantly (because the effect of fluid loading on the structure is neglected) and hence the fluid displaced by the piezoelectric actuator directly flows into the sorting region. On the other hand, in the 'Fully coupled' approach (blue curve), the fluid displaced by the piezoelectric actuator is partially housed in the volume made available by the PDMS cylinder deformation. The streamline rotation angle θ turns out to be sinusoidal, as the sample stream rotation obtained experimentally (see also **Figure S2**). The comparison of the 'Hybrid' approach (blue curve) with the 'Fully coupled' approach (red curve) shows that full coupling should be considered even on the metal plate.
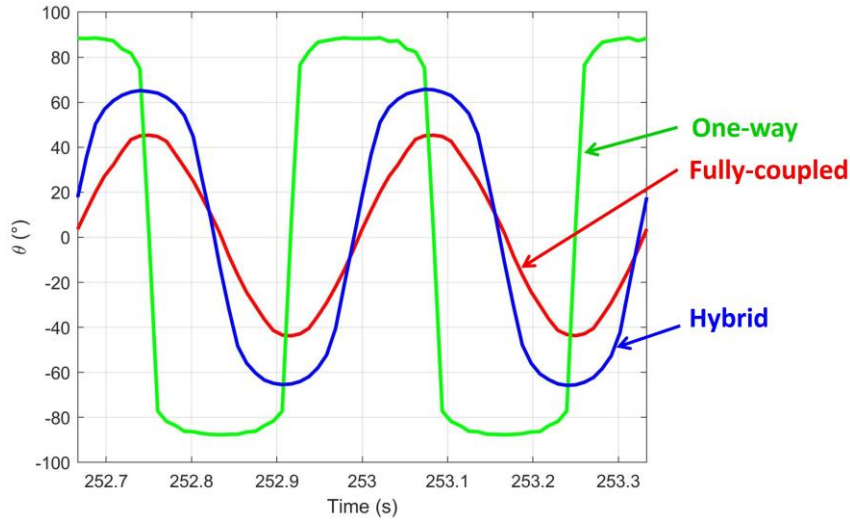

Figure S1. Rotation angle $\theta(t)$ of the central streamline obtained with 'Fully coupled' (red curve), 'One-way' (green curve), and 'Hybrid' (blue curve) coupling modalities (sinusoidal actuation, 10 V_{pp}, 3 Hz).

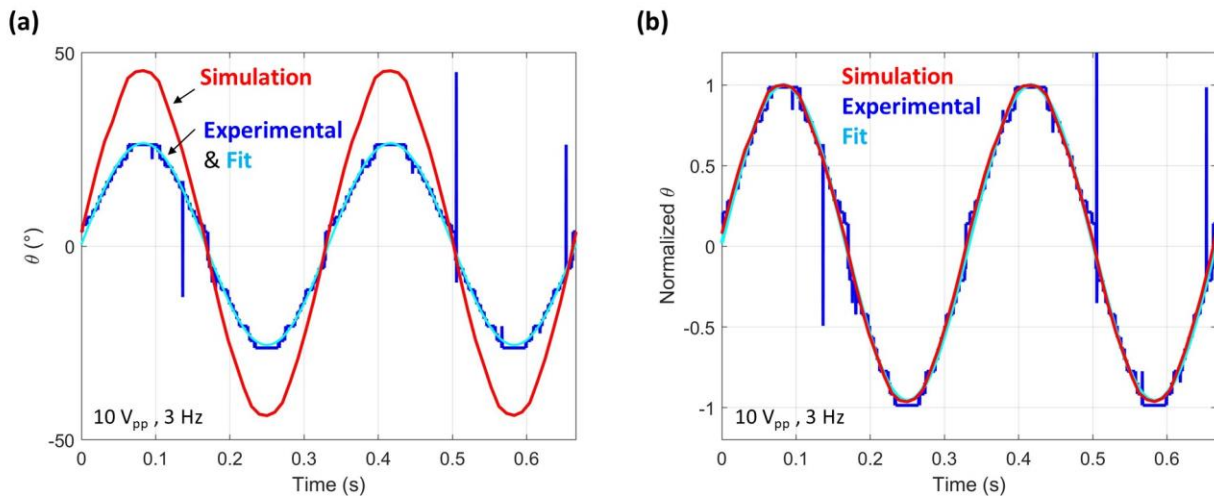## 2. Comparison of (fully coupled) simulation results and experimental results

Figure S2. Sinusoidal drive signal (10 V_pp, 3 Hz). (a) Rotation angle of the central streamline obtained with the fully coupled simulation (red curve) and rotation angle of the sample stream obtained via image processing of the experimental video (raw data, blue curve; fitted sinusoid, cyan curve). (b) Rotation angles normalized with respect to their amplitude.
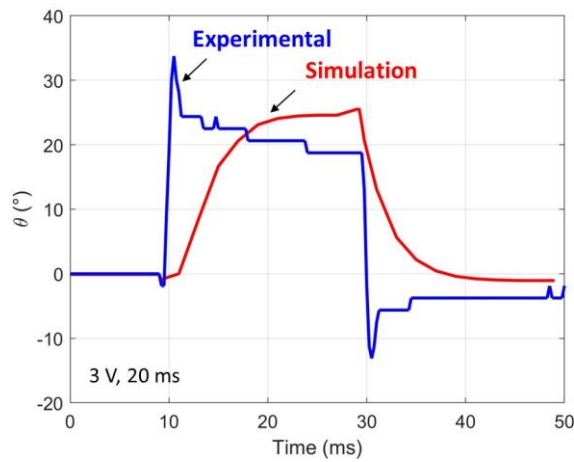

Figure S3. Pulse drive signal (3 V, 20 ms). Rotation angle of the central streamline obtained with the fully coupled simulation (red curve) and rotation angle of the sample stream obtained via image processing of the experimental video (blue curve).

3. Supplementary videos description

Video S1: Sinusoidal actuation case (3 Hz, 10 V_{pp}). The video was recorded at 4000 fps. To reduce the size of the file, it was then subsampled at 200 fps. The reproduction frame rate is set to 20 fps (10× slow down). Three actuation cycles are shown. Polystyrene beads (5 µm diameter) were suspended in the sample stream, to show particle deflection into the different outlets.

Video S2: Pulse actuation case (pulse duration $T_{on} = 10$ ms, repetition period $T = 66$ ms, 5 V). The video was recorded at 4000 fps. To reduce the size of the file, it was subsampled at 800 fps. The reproduction frame rate is set to 20 fps (40× slow down). Three pulses are shown. As future work, an impedance sensor will be integrated into the device to synchronize pulse activation with particle passage.